Ca²⁺ permeation through C-terminal cleaved, but not full-length human Pannexin1 hemichannels, mediates cell death

Magdiel Salgado[a,1] (ID), Valeria Márquez-Miranda[b], Luciano Ferrada[c], Maximiliano Rojas[b] (ID), Gonzalo Poblete-Flores[d], Fernando D. González-Nilo[a,b,1], Álvaro O. Ardiles[a,d] (ID), and Juan C. Sáez[a,1]

Pannexin1 hemichannels (Panx1 HCs) are found in the membrane of most mammalian cells and communicate the intracellular and extracellular spaces, enabling the passive transfer of ions and small molecules. They are involved in physiological and pathophysiological conditions. During apoptosis, the C-terminal tail of Panx1 is proteolytically cleaved, but the permeability features of hemichannels and their role in cell death remain elusive. To address these topics, HeLa cells transfected with full-length human Panx1 (fl-hPanx1) or C-terminal truncated hPanx1 (Δ371hPanx1) were exposed to alkaline extracellular saline solution, increasing the activity of Panx1 HCs. The Δ371hPanx1 HC was permeable to DAPI and Etd⁺, but not to propidium iodide, whereas fl-hPanx1 HC was only permeable to DAPI. Furthermore, the cytoplasmic Ca²⁺ signal increased only in Δ371hPanx1 cells, which was supported by bioinformatics approaches. The influx of Ca²⁺ through Δ371hPanx1 HCs was necessary to promote cell death up to about 95% of cells, whereas the exposure to alkaline saline solution without Ca²⁺ failed to induce cell death, and the Ca²⁺ ionophore A23187 promoted more than 80% cell death even in fl-hPanx1 transfectants. Moreover, cell death was prevented with carbenoxolone or ¹⁰Panx1 in Δ371hPanx1 cells, whereas it was undetectable in HeLa Panx1⁻/⁻ cells. Pretreatment with Ferrostatin-1 and necrostatin-1 did not prevent cell death, suggesting that ferroptosis or necroptosis was not involved. In comparison, zVAD-FMK, a pan-caspase inhibitor, reduced death by ~60%, suggesting the involvement of apoptosis. Therefore, alkaline pH increases the activity of Δ371hPanx1HCs, leading to a critical intracellular free-Ca²⁺ overload that promotes cell death.

Pannexin1 | hemichannel | cell death | Ca²⁺ influx

Pannexin (Panx) proteins belong to a family integrated by three members (Panx1-3) (1) among which Panx1 is characterized by a widespread expression (2). Consequently, Panx1 is present in a variety of cell types within both the central and peripheral nervous systems as well as in numerous other organs. This widespread distribution suggests a critical role in diverse tissue functions (3). In mammalian cells, Panx1 hemichannels (Panx1 HCs)—which constitute half of a gap junction channel (4)—are made up of seven protein subunits (5), forming membrane pores that facilitate communication between the intracellular and extracellular spaces. Panx1 HCs are nonselective membrane channels that allow the passage of monovalent ions and small molecules, metabolites, and autocrine and paracrine signals (6–9).

In physiological responses, connexin hemichannels (Cx HCs) can open under controlled conditions without compromising cell survival (8, 10, 11). However, an increase in their activity in cells experiencing pathological conditions, such as hypoxia–reoxygenation or mutations that result in increased activity, can accelerate, or even cause cell death (12–17). Additionally, cell leakage via Cx HCs of vital intracellular molecules such as reduced glutathione (GSH) and adenosine triphosphate (ATP) may contribute to promoting cell death (18, 19). However, there is no known evidence that links Panx1 HC permeants with the onset of cell death.

Regarding cell death, the calcium ion (Ca²⁺) plays a crucial role as it activates numerous intracellular metabolic pathways, including Ca²⁺-dependent proteases, lipases, and nucleases (20–22). Moreover, Ca²⁺ has been extensively studied in various forms of cell death due to its involvement in many cellular processes that are related to either initiation or execution of cell death along with the activation of intracellular signaling pathways (23–25). For instance, an elevation in intracellular free-Ca²⁺ is recognized as a hallmark in ferroptosis, wherein Ca²⁺ flux through ferroptotic nanopores plays a relevant role (24). As in ferroptosis, in necroptosis and pyroptosis, membrane perturbations induce an influx of ions, including Ca²⁺, before cellular lysis (26, 27). However, in both cases, intracellular Ca²⁺ elevation occurs before the plasma membrane bursts (26, 28), suggesting that additional mechanisms may facilitate Ca²⁺ uptake in compromised cells. In this regard, it has been demonstrated that some Cx HCs are Ca²⁺ permeable, such as those formed by Cx26

Significance

During apoptosis, the C-terminal tail of the protein subunits of human Pannexin1 hemichannels (hPanx1 HCs) undergoes cleavage, which has been proposed to affect the permeability of the hemichannels to different molecules or ions. In this work, we demonstrate that activation of cleaved hPanx1 HCs allowed Ca²⁺ influx into cells, which does not occur with full-length hPanx1 HCs. Interestingly, Ca²⁺ influx through cleaved hPanx1 HC was sufficient to induce cell death in the absence of another cell death stimulus, a phenomenon which largely depended on hPanx1 HC activity. Thus, hPanx1 HCs cleavage and activity could be a relevant target to modulate of cell death.

Author affiliations: ªInstituto de Neurociencias, Centro Interdisciplinario de Neurociencias, Universidad de Valparaíso, Valparaíso 2381850, Chile; ᵇCenter for Bioinformatics and Integrative Biology, Facultad de Ciencias de la Vida, Universidad Andrés Bello, Santiago 8370146, Chile; ᶜCentro de Microscopía Avanzada-Biobío, Universidad de Concepción, Concepción 4070386, Chile; and ᵈEscuela de Medicina, Facultad de Medicina, Universidad de Valparaíso, Valparaíso 2341386, Chile

¹To whom correspondence may be addressed. Email: magdiel.salgado@cinv.cl, fernando.gonzalez@unab.cl, or juancarlos.saez@uv.cl.
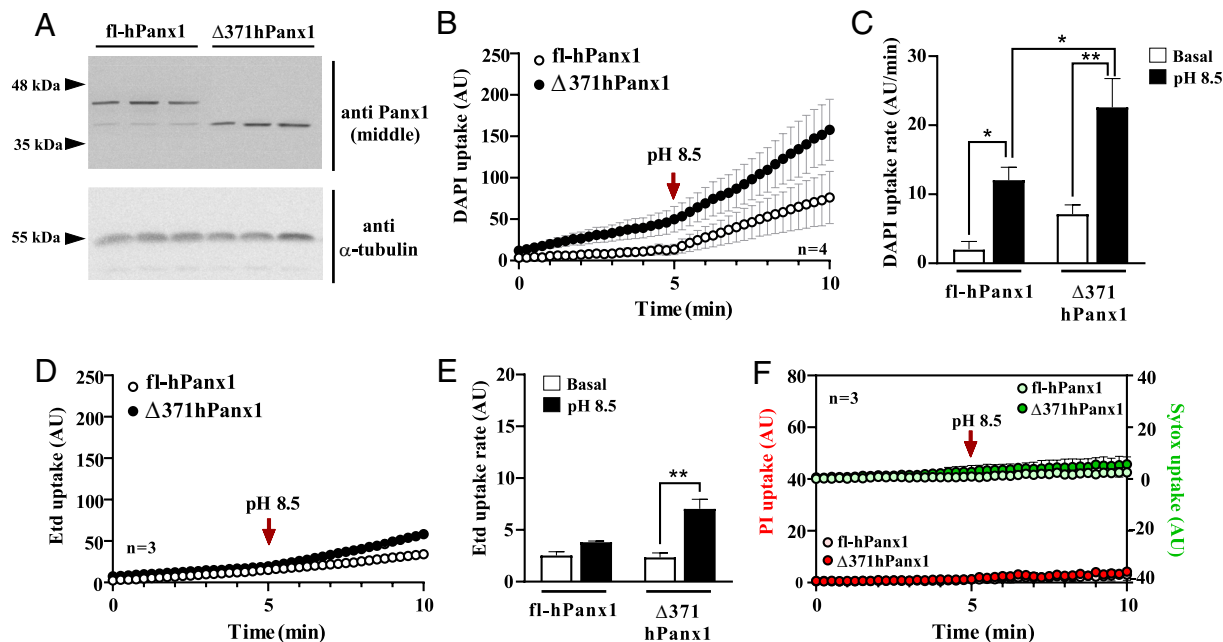
Fig. 1. C-terminal truncation on hPanx1 allows increased permeability to DAPI and Etd+ but not PI. (*A*) Immunodetection of full-length and C-terminal truncated hPanx1 in HeLa Cx45/Panx1 double KO cells transfected with a bicistronic vector (IRES) carrying each cDNA and a reporter. α-tubulin was used as a loading control. (*B*) Both fl and Δ371hPanx1 HC increased their activity in response to alkaline pH (8.5) but to a greater extent the truncated isoform, n = 4. (*C*) Dye uptake rates from (*B*). (*D* and *E*) Etd+ uptake rate only increases in HeLa cells transfected with Δ371hPanx1 in response to alkaline pH, n = 3. (*F*) Neither full-length nor truncated hPanx1 HCs allow the flow of PI nor Sytox dyes. Data are presented as Mean ± SEM. *$P \leq 0.05$; **$P \leq 0.01$.

or Cx43 (29, 30). Although some studies have extrapolated the Ca^{2+} permeability of Panx1 HCs present in the sarcoplasmic reticulum (31) to that of cell membrane hemichannels, to our knowledge, only a few studies have addressed this issue (32), but a direct demonstration of this matter remains elusive.

During apoptosis, ATP and uridine triphosphate (UTP) are released to the extracellular space, which is blocked by carbenoxolone (CBX) and probenecid, inhibitors of Panx1 HCs. However, despite the reduction of monocyte recruitment, Panx1 HC inhibition or knockdown did not affect apoptosis progression (33). In this study, Panx1 was identified as a target for Casp3/7, which cleaves the C-terminal tail of immunoprecipitated hPanx1 and enhances its activity. Consequently, the C-terminal tail was reported to have an autoinhibitory effect on the central pore of hemichannels formed by truncated hPanx1 (34). Furthermore, it has been shown that Casp11 can also cleave mPanx1 in macrophages undergoing lypopolysacharide-induced pyroptosis (35). However, it remains to be seen whether this cleavage occurs by inducing apoptosis in cultured cells and whether this state allows the influx of Ca^{2+}, favoring this or other forms of cell death. In this study, we generated a truncated form of hPanx1 (Δ371hPanx1) and transfected it into HeLa cells to evaluate permeability, Ca^{2+} flux, and cell death caused by elevated hemichannel activity. In these cleaved hemichannels, we found a close correlation between these parameters, which was absent in cells transfected with full-length hPanx1.

Results

Hemichannels Formed by Truncated hPanx1 Are More Permeable than Those Formed by Wild-Type hPanx1. The C-terminal tail of hPanx1 has been proposed to act as an intramolecular inhibitor of Panx1 HCs, which may be cleaved during apoptosis (34). However, the permeability properties of hemichannels formed by the truncated form have not been completely characterized. To advance our understanding, we generated a truncated hPanx1 by

including a stop codon immediately after Gly371 and cloned it in a bicistronic vector (pIRES2GFP). After transfection, western blot analyses using an antibody against the middle of hPanx1, revealed a band of about 38 kDa (Fig. 1*A*), closely matching the predicted molecular weight of the truncated hPanx1 (Δ371hPanx1). This contrasts with the 45 kDa band detected in cells transfected with a bicistronic vector carrying full-length hPanx1 (fl-hPanx1) (Fig. 1*A*).

To evaluate some permeability properties of Δ371hPanx1 HCs, we conducted DAPI (+2 net charge and 350.2 g/mol) uptake assays in real time. As this dye only permeates the cell membrane through hemichannels, nuclear fluorescence is proportional to hemichannel activity (36–38). The hemichannel activity of both isoforms quickly increased by exposing the HeLa transfectants to an alkaline saline solution (Fig. 1*B*), which has been reported to increase the activity of mouse Panx1 HCs (32). Maximal hPanx1 HC activity was induced by pH 8.5 (*SI Appendix*, Fig. S1), and the increased activity was reverted by Krebs solution pH 5.5 (*SI Appendix*, Fig. S2 *A and B*). Interestingly, there was no response to pH 5.5 in Δ371hPanx1 cells (filled circles). Additionally, while the activity of fl-Panx1 HCs was increased further upon mechanical stress stimulation after applying pH 8.5, Δ371hPanx1 cells did not show enhanced dye uptake upon stretch stimulation (*SI Appendix*, Fig. S2 *C and D*). This suggests that both acidic-induced deactivation and stretching-induced activation are dependent on the C-terminal tail of hPanx1, targeting specific gating mechanisms. Our results demonstrated that in fl-hPanx1 transfectants, the DAPI uptake rate increased from 2.0 ± 0.9 to 12.0 ± 1.9 AU/min, $P = 0.045$, in response to alkaline solution. Conversely, in Δ371hPanx1, this value increased from 7.1 ± 1.3 to 22.6 ± 2.9 AU/min, $P = 0.004$ (Fig. 1 *B and C*). Moreover, the dye uptake rate in Δ371hPanx1 transfectants was significantly higher than fl-hPanx1 in response to alkaline pH, $P = 0.044$ (Fig. 1*C*). Although Δ371hPanx1 cells showed a relatively high dye uptake under basal conditions, this was not significantly different from that obtained by fl-hPanx1 under the same condition ($P = 0.478$).
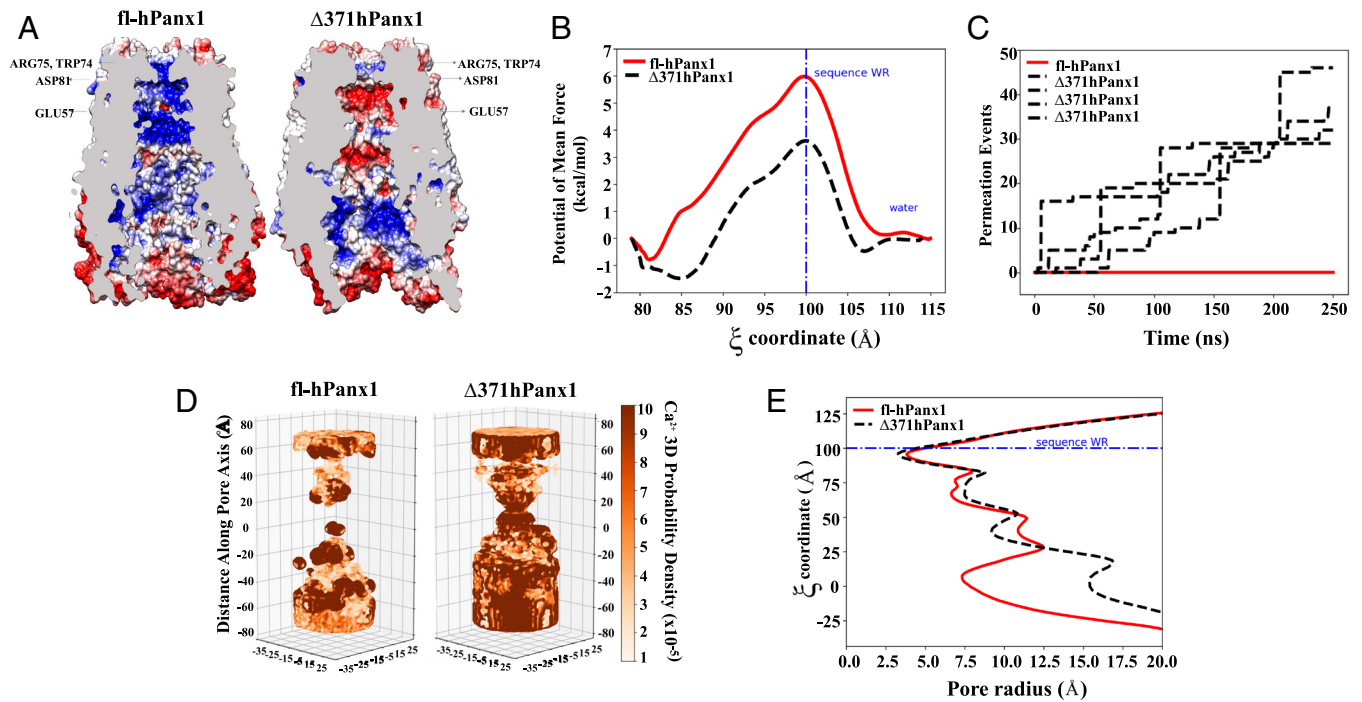
Fig. 2. Truncated, but not full-length hPanx1 is energetically favored for the Ca^{2+} passage. (A) Electrostatic potential of full-length Panx1 hemichannel (*Left*, fl-hPanx1) vs. C-terminal truncated hemichannel (*Right*, Δ371hPanx1). (B) Free energy profile for the passage of Ca^{2+} for Panx1 HCs variants. (C) Number of permeation events for full-length (red line) and CT truncated hPanx1 HC (black line). (D) Ca^{2+} ion probability density of full-length (*Left*) and C-terminal truncated hPanx1 (*Right*). (E) Pore dimension of Panx1 hemichannel variants through HOLE software.

Ethidium (Etd+) bromide (+1 net charge and 394.3 g/mol) has been extensively used to evaluate murine hemichannel activity, but its flow through hPanx1 HCs remains understudied. We found that the Etd+ uptake in fl-hPanx1 cells was very low either under basal conditions or in response to alkaline pH (Fig. 1*D*, empty circles). A similar Etd+ uptake in Δ371hPanx1 cells compared with fl-hPanx1 cells was obtained in basal conditions (Fig. 1*E*). However, a significant increase in Etd+ uptake rate was recorded in Δ371hPanx1 HeLa cells in response to Krebs pH 8.5 (from 2.5 ± 0.3 to 7.3 ± 0.8 AU/min, $P = 0.007$) (Fig. 1 *D* and *E*). Despite this rise, the maximal uptake rate of Etd+ was approximately 1/3 of that obtained with DAPI (Fig. 1*E* vs. Fig. 1*C*, fourth bar, similar transfection efficiency). Finally, we ask ourselves whether this change in permeability observed in Δ371hPanx1 HCs could allow the permeation of bigger dyes, such as propidium iodide (PI, molecular weight of 668 g/mol and a charge of +2). We found that neither fl nor Δ371hPanx1 HCs were significantly permeable to this dye, either at physiologic or alkaline pH (Fig. 1*F*). Thus, Δ371hPanx1 HCs are more permeable to DAPI and Etd+, compared to fl-hPanx1 HCs.

C-Terminal Cleavage of hPanx1 Allows Ca^{2+} Flow through Hemichannels. Since it is still under discussion whether Ca^{2+} permeates Panx1 HCs (32, 39), we studied the energetics of the translocation of a Ca^{2+} ion along fl-hPanx1 and Δ371hPanx1 HCs. The umbrella sampling method was applied to obtain a free energy profile of Ca^{2+} crossing from the uppermost section of the protein to the pore, until reaching residue Glu57 in both proteins. Additionally, electrostatic potential maps enable the visualization of changes resulting from residue deletions in the truncated hemichannel. In both hemichannel maps, an electropositive potential derived from the presence of Arg75 residues accompanied by Trp74 is evident, with a slightly more pronounced effect in fl-hPanx1 HC (Fig. 2*A*). However, the energy barrier for Ca^{2+} to reach the intracellular region is nearly 3 kcal/mol higher in fl-hPanx1 HC compared to Δ371hPanx1 HC (Fig. 2*B*).

According to the electrostatic potential maps, the region flanked by Asp 81 and Glu 57 residues forms a section (reaction coordinate ξ between 80 and 90), which in the case of Δ371hPanx1 HC appears significantly electronegative. fl-hPanx1 HC, on the other hand, appears strongly electropositive, extending further toward the intracellular side, favoring the flow of anions, as previously proposed (40). This is also consistent with the hPanx1 HC electrostatic potential recently reported (41), finding only slight differences as a result that our potential electrostatic maps were obtained after submitting the models to MD simulations. The presence of this electronegative region in the Δ371hPanx1 HC creates conditions for a reduced energy barrier during the cation passage. All of this suggests a long-range effect in the selectivity filter promoted by the hPanx1 residues that were removed in the Δ371hPanx1 HC. The greater probability of cation passage obtained in Δ371hPanx1 is in direct accordance with the greater permeability to either DAPI or Etd+, which have a net charge of +2 and +1, respectively. However, other aspects, such as the molecular shape, could also be involved in the passage of DAPI through the pore, given that activating fl-hPanx1 at alkaline pH significantly enhances its permeability, despite the electropositive environment. Furthermore, the presence of an electronegative zone between Asp81 and Glu57 corresponds to the energy well (2 kcal/mol) experienced by Ca^{2+} during its passage through the truncated HC (ξ = 85), which differs from the observation in the fl-hPanx1 HC.

To further evaluate the Ca^{2+} permeation, we performed MD simulations on fl-hPanx1 and Δ371hPanx1 HCs, and we estimated the number of Ca^{2+} permeation events and Ca^{2+} density probability. Four consecutive 250-ns MD simulations generated permeation events in the truncated hPanx1, but no Ca^{2+} permeation was observed in the fl-hPanx1 HC (Fig. 2*C*), indicating that Ca^{2+} ions can transit through the pore channel only when the C-terminal is absent. As in the energetic and electrostatic potential analysis, the application of an external potential field also revealed
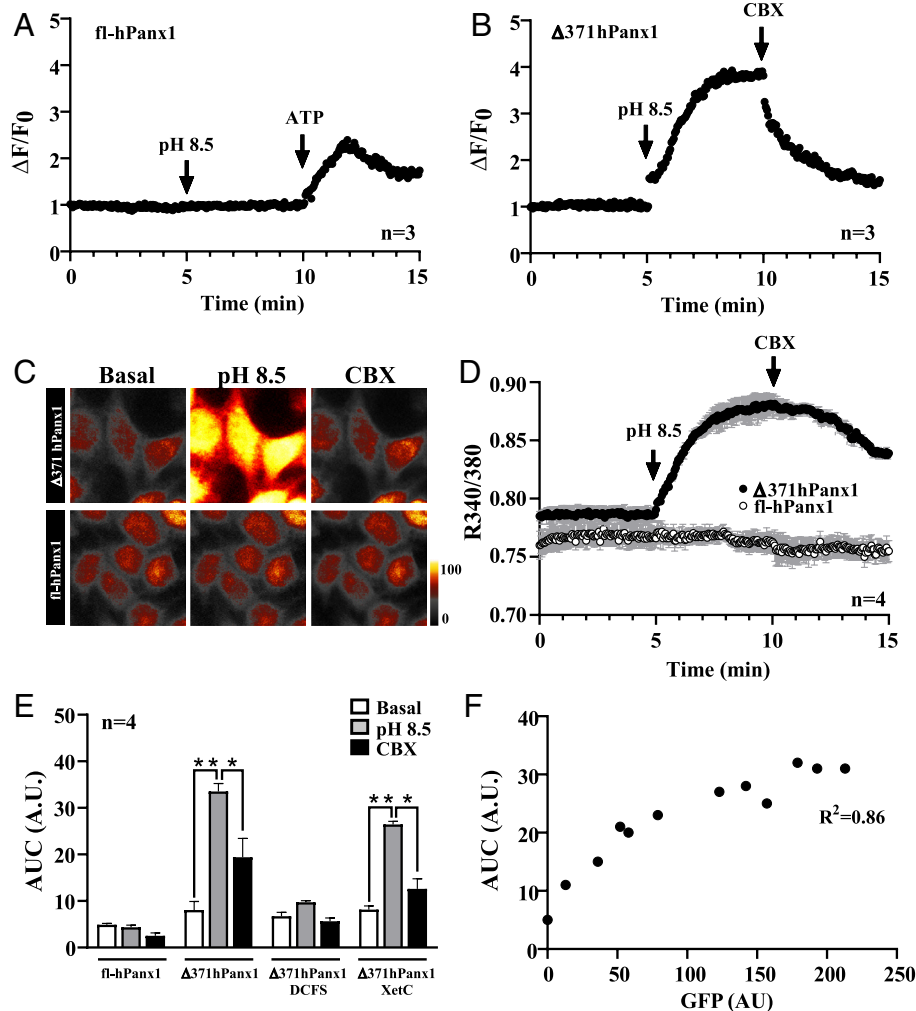
Fig. 3. C-terminal truncation on hPanx1 indeed allows Ca^{2+} influx through hemichannels. (*A*) Cx45/Panx1 KO HeLa cells were cotransfected with fl-hPanx1 and Lck-GCaMP3 and Ca^{2+} transients were evaluated by fluorescence live cell time-lapse in response to pH 8.5. ATP was used for activating purinergic ionotropic receptors, n = 3. (*B*) Similarly, Lck-GCaMP3 and Δ371hPanx1 were transfected, showing a rapid increase in GCamP3 signal when hemichannels were activated with alkaline pH, which was blocked with CBX, n = 3. (*C* and *D*) By using Fura-2, previous results were confirmed, showing that alkaline pH only allows an increase in Fura ratio in truncated hPanx1 transfectants, but not with fl-hPanx1 isoform. CBX partially inhibited the calcium signal evaluated with Fura-2. All recordings were made in the presence of 1 mM Na_3VO_4, a Ca^{2+} pump blocker, n = 4. (*E*) The area under the curve (AUC in arbitrary units: A.U.) showed a significant increase in response to alkaline pH only in Δ371hPanx1 transfectants. This response was not affected in the presence of Xestospongin C (XetC), an IP_3R antagonist but was almost completely suppressed by DCFS, n = 4. (*F*) There is a high correlation ($R^2 = 0.86$) between the expression level of Δ371hPanx1 and the response of hemichannels to alkaline pH recorded with Fura-2. *$P \leq 0.05$, **$P \leq 0.01$.

a higher Ca^{2+} density in the pore of the truncated hPanx1 than in the pore of the full-length channel. In the full-length Panx1 HC, a density gap of Ca^{2+} was observed in the center of the pore between 0 and 20 Å on the z-axis, whereas the presence of the ion was observed throughout the entire pore in the truncated hPanx1 HC with a high density in the center, showing a greater ion occupancy (Fig. 2*D*). In accordance with the above changes, the pore radius obtained in truncated hPanx1 is approximately 8 Å bigger than in fl-hPanx1 HC considering the cavity space (close to ξ = 0) (Fig. 2*E*). Therefore, these results strongly suggest that Ca^{2+} could flow through truncated but not fl-hPanx1 HCs.

To experimentally test this, we evaluated intracellular Ca^{2+} transients by two methods. In one of them, we used the membrane-targeted Ca^{2+} indicator Lck-GCaMP3 (42), which was cotransfected with either fl-hPanx1 or Δ371hPanx1. In fl-hPanx1 transfectants, the increase in HC activity induced by alkaline pH did not alter the fluorescence associated with Lck-GCaMP3. In contrast, the application of 0.5 mM ATP was sufficient to evoke a ~twofold increase of this signal, likely indicative of a purinergic response (Fig. 3*A*). On the other hand, the increased activity of Δ371hPanx1

HCs favored a rapid and stable increase in the submembranous Ca^{2+} signal (Fig. 3*B*). It should be noted that despite of a higher basal permeability to DAPI of Δ371hPanx1 HCs (Fig. 1*C*), there were no changes in Ca^{2+} signal associated with Lck-GcamP3 until the activity of HCs was increased with alkaline pH (Fig. 3*B*). Furthermore, this signal was almost completely reverted by 10 μM CBX. Second, we used the Ca^{2+} indicator Fura-2 and repeated the recording protocol for both isoforms. Again, the increase in fl-hPanx1 HC activity upon alkaline pH was not associated with a significant change in cytoplasmic Ca^{2+} signal (*SI Appendix*, Fig. S3). However, in HeLa-Δ371hPanx1 cells, the exposure to alkaline pH caused a rapid and transitory increase in this signal (*SI Appendix*, Fig. S3). To enhance the Ca^{2+} signal with Fura-2, cells were treated with 1 mM sodium orthovanadate, a Ca^{2+} pump inhibitor (43), to favor Ca^{2+} retention within the cell. Under these conditions, the increase in Δ371hPanx1 HC activity induced by alkaline pH caused a rapid and sustained increase over time in Ca^{2+} signal, whereas no detectable changes were observed in fl-hPanx1 transfectants subjected to the same treatment (Fig. 3 *C* and *D*). As observed with the Lck-GcamP3 protein, the Ca^{2+} signal was inhibited by CBX

when evaluated with Fura-2 (Fig. 3D). A significant increase (three-fold) in the AUC was obtained only in Δ371hPanx1 cells in response to alkaline pH (Fig. 3E). When we assayed this response in divalent cation-free solution (DCFS), no response was generated, indicating that extracellular Ca^{2+} entry is required (Fig. 3E). On the contrary, preincubation with xestospongin C (XetC) did not significantly affect the response to pH 8.5, suggesting that Ca^{2+} release from intracellular stores is not involved in this phenomenon (Fig. 3E). Finally, we calculated the fluorescence intensity of the reporter GFP and plotted it against the AUC achieved in response to alkaline pH and obtained a high correlation between these parameters (R^2 = 0.86), strongly suggesting that Ca^{2+} entrance depends on Δ371hPanx1 expression and most likely on hemichannel activity elicited by this protein.

Ca^{2+} Influx through Δ371hPanx1 Hemichannels Lead to Cell Death. It has been proposed that Panx1 cleavage occurs during apoptosis since hPanx1-GFP immunoprecipitated fusion protein is truncated when incubated with active caspase 3 (33). However, it remains elusive whether this occurs naturally in apoptotic cells and whether apoptosis depends on Ca^{2+} influx via truncated hemichannels. Therefore, we first evaluated whether hPanx1 is indeed proteolyzed in dying cells and whether this process can occur by increasing the activity of fl-hPanx1 HCs. To this end, Panx1$^{-/-}$ HeLa cells were transfected with an fl-hPanx1 construct and after 24 h were incubated for 4 h with Krebs pH 8.5 or treated with TNF-α 50 μg/mL in the absence of FBS for 24 h to induce apoptosis (44). We evaluated Panx1 cleavage by immunoblotting (Fig. 4A) and found a significant increase in cleaved (38 kDa) vs. full-length (45 kDa) hPanx1 in TNF-α treated cells (Fig. 4B), demonstrating that the cleavage occurs when extrinsic apoptosis is activated. Treatment with 5 μM A23187, a Ca^{2+} ionophore, promoted a significant increase in cleaved hPanx1, suggesting that Ca^{2+} influx bypassing HCs is sufficient to promote Panx1 cleavage (Fig. 4A, lane 3 and Fig. 4B). Active Casp3 was detected mainly in A23187 and TNF-α treated cells but to a much lesser extent in cells exposed to pH 8.5 in which no significant cleavage of Panx1 was detected (Fig. 4A). Interestingly, dye uptake was not significantly affected under treatment with TNF-α nor in cells transfected with the truncated form in the absence of stimulus. In contrast, an alkaline solution induced a significant increase in dye uptake in both fl-hPanx1 and Δ371hPanx1 cells (Fig. 4C). Similar results were obtained in fl-mPanx1 HeLa cells, demonstrating that this mechanism is conserved between both species (*SI Appendix*, Fig. S4).

Sandilos et al. proposed that under apoptosis cleaved hPanx1 HCs present greater activity (34). However, the outcomes following this or after treatment with another death stimuli remain unknown. For this reason, we subsequently focused on studying how cell viability is influenced by enhanced Δ371hPanx1 HC activity induced with pH 8.5 in healthy cells. As a control, we also performed this analysis in Panx1-KO and fl-hPanx1 HeLa cells. Furthermore, each study was made in the absence or presence of extracellular Ca^{2+} (3 mM) and at pH 7.4 or 8.5. Utilizing the Incucyte real-time monitoring system, we followed the cell death under each condition over 4 h, determined by cell labeling with PI or Sytox, which do not significantly permeate wild type or truncated Panx1 HCs (Fig. 1F). In fl-hPanx1 cells, cell death was very low and did not suffer evident changes in response to pH 8.5, regardless of the presence of extracellular Ca^{2+} (Fig. 4D). However, in Δ371hPanx1 cells, a clear increase in cell death (PI$^+$) was observed only at alkaline pH in the presence of extracellular Ca^{2+} (Fig. 4E). Automatic quantification of cell death (% Sytox or % PI/total cells) after 4 h treatment showed that in fl-hPanx1 cells, the percentage of dead cells was less than 8%, without significant

variations between the different conditions (Fig. 4F). In contrast, a significant elevation in cell death was achieved from 3rd hour in Δ371hPanx1 cells treated with alkaline pH and only in the presence of extracellular Ca^{2+} (Fig. 4G, green line, 95% cell death for 4 h). Interestingly, PI labeling was significantly reduced by preincubation with N-Benzyloxycarbonyl-Val-Ala-Asp(O-Me) fluoromethyl ketone (zVAD-FMK), a caspase inhibitor, from 94.7 ± 10.7% to 39.4 ± 0.6%, P = 0.0012 (Fig. 4H), suggesting apoptosis activation. Oxidative stress was partially involved as Trolox application significantly reduced cell death to 58.8% only after 4 h (P = 0.0332). Contrarily, preincubation with neither Nec-1s nor Fer-1 significantly affected the rate of cell death (Fig. 4H), suggesting that necroptosis and ferroptosis do not play significant roles in the death observed after activating hemichannels in the presence of extracellular Ca^{2+}. None of the cell death inhibitors described above affected Sytox staining in fl-hPanx1 HeLa cells at any condition or in the absence of inhibitors after 4 h treatment, as well as in Panx1-KO cells (*SI Appendix*, Fig. S5). In Δ371hPanx1 cells preincubated with Panx1 HCs inhibitors, cell death was drastically reduced, highlighting a key role of these hemichannels in this phenomenon (*SI Appendix*, Fig. S6).

In agreement with the activation of Casp3 and cleavage of Panx1 observed in cells treated with A23187, this drug induced a pH-independent significant increase in cell death even in cells transfected with fl-hPanx1, but only in the presence of extracellular Ca^{2+} (*SI Appendix*, Fig. S7). Finally, we evaluated whether mortality observed in cells transfected with Δ371hPanx1 occurs with increased ROS production. Although we found that the production of ROS in the different conditions evaluated was relatively low, it was slightly higher upon exposure to alkaline pH in the presence of Ca^{2+} after 4 h treatment, suggesting that ROS are poorly involved in evoking cell death, but they play a more relevant role in the long term (Fig. 4I). This is consistent with the effect of Trolox that reduced about 60% cell death after 4 h treatment (Fig. 4H, pink bar). Taken together, these results demonstrate that Ca^{2+} influx, whether through cleaved Panx1 or indirectly favored by Ca^{2+} ionophore, promotes the development of apoptosis, favoring proteolytic Panx1 cleavage. Additional research is necessary to study how intracellular Ca^{2+} itself enhances Panx1 cleavage, but since it favors the activation of Casp3 (Fig. 4A), it is most likely the underlying mechanism.

Discussion

In this study, we demonstrated that the activation of Panx1 HCs by extracellular alkaline pH allows the influx of Ca^{2+} but only when the C-tail is cleaved. Remarkably, this Ca^{2+} influx was crucial for inducing cell death, which depends on caspase activity and partially on oxidative stress. None of these phenomena were observed in HeLa cells transfected with fl-hPanx1 nor in Panx1-KO cells, which did not show a significant increase in cytoplasmic Ca^{2+} upon exposure to alkaline pH.

Upon exposure to pH 8.5, an increased hemichannel activity was previously demonstrated in HeLa-Cx43 (29) and mPanx1-HCs (32). Here, this phenomenon was also shown for hPanx1 HCs, with a greater response when C-tail was absent. Although the mechanism by which pH 8.5 increases the activity of hemichannels is still unknown, for Cx43, this response was explained by an increment in the opening probability of hemichannels rather than an increase in protein levels at the cell membrane, as alkaline extracellular solution induced an increase in Cx43 mediated currents without significant change in levels of Cx43 in the plasma membrane (29). We have shown that almost immediately after exposure to pH 8.5, cells transfected with hPanx1 (full-length or
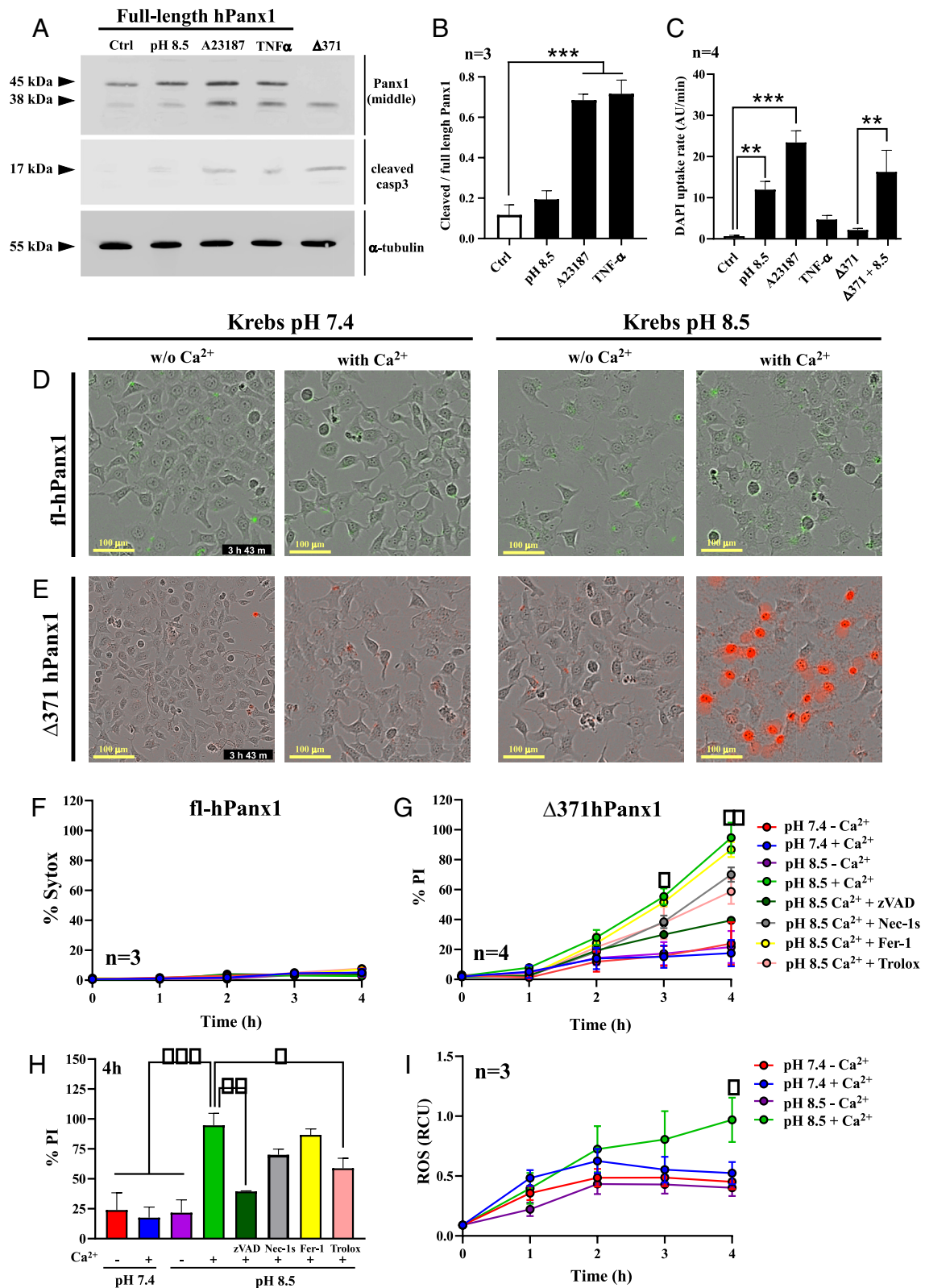
Fig. 4. Ca²⁺ influx through truncated hPanx1 leads to cell death. (*A*) HeLa cells transfected with full-length hPanx1 were incubated for 4 h with Krebs pH 8.5 (lane 2), 5 μM A23187 (lane 3), or 50 μg/mL TNF-α (lane 4). Other cells were 48 h-transfected with Δ371hPanx1 vector, and proteins were extracted and loaded for western blot analysis (lane 5). (*B*) Densitometric analysis was performed and truncated/full-length Panx1 was plotted for each condition, n = 3. (*C*) DAPI uptake rates from each condition, n = 4. (*D*) Sytox staining (green) in HeLa cells transfected with hPanx1, varying either pH of Krebs solution or presence of 3 mM Ca²⁺ after 4 h. (*E*) PI staining (red) in HeLa cells transfected with Δ371hPanx1, varying either pH of Krebs solution or presence of 3 mM Ca²⁺ after 4 h. (*F*) Percentage Sytox staining in fl-hPanx1 was not affected by extracellular pH or presence of extracellular Ca²⁺. Consequently, this staining was not altered by cell death inhibitors, n = 3. (*G*) Percentage PI staining in Δ371hPanx1 transfectants changing pH, presence of extracellular Ca²⁺ and preincubation with Ferrostatin-1 (Fer-1), necrostatin-1s (Nec-1s), zVAD, or Trolox, n = 4. (*H*) Percentage PI staining in Δ371hPanx1 HeLa cells following a 4 h incubation with pH 7.4 or 8.5, in the absence or presence of extracellular Ca²⁺. PI staining was also plotted when different cell death inhibitors were preincubated, as depicted in legend. (*I*) ROS determination in Δ371hPanx1 transfectants changing extracellular pH or Ca²⁺ presence, n = 3. Data are presented as Mean ± SEM. *$P \le 0.05$; **$P \le 0.01$; ***$P \le 0.001$.

cleaned) allow a significant increase in DAPI uptake, making it impossible for this response to be a transcriptional event. However, a 30% increase in the total level of Panx1 was observed in HeLa-hPanx1 cells incubated with Krebs pH 8.5 for 4 h (Fig. 4*A*, lane 2), opening the possibility of transcriptional regulation in this time scale. Additional studies are necessary to determine whether hPanx1 expression or protein degradation is affected.

Panx1 HCs from zebrafish have been proposed to act as pH sensors, increasing dye uptake in response to increased pH (8.0) (45). In the present work, we have shown that a similar regulation can take place for hPanx1, which allows us to speculate the existence of tissue microenvironments where this hemichannel has a maximal open probability under physiological conditions, such as the matrix of the pancreas (pH 8.8) or the gallbladder (pH 8.2) (46). Interestingly, while acidification reduces the activity of fl-hPanx1 HCs, Δ371hPanx1 HCs were unaffected (*SI Appendix*, Fig. S2). Therefore, it seems that regulation by acidic pH does not simply antagonize alkaline pH, but most likely its inhibitory function depends on the C-terminal tail of hPanx1. Similarly, this truncated form of hPanx1 loses its regulation by mechanical stress (*SI Appendix*, Fig. S2), which, at least in the mouse orthologous protein, is the Ser394 residue (C-tail), a target of the Piezo/Ca^{2+}/CaMKII axis (47). It remains unknown and an important project to study whether other classical stimuli, such as increased intracellular Ca^{2+}, increased extracellular K$^+$, or depolarization, have different effects over Δ371hPanx1 HCs from those observed on fl-hPanx1 HCs. Considering our molecular simulations, the energy barrier to open a truncated hemichannel is half that of the fl-Panx1 HC, which makes it plausible to speculate that the power of the stimulus should be lower. Future studies will help us clarify this issue.

Regarding Etd+ influx, our results differ from the previous report which indicated that this dye permeates cleaved and fl-hPanx1 in response to alkaline pH. There were no differences in permeability concerning Δ378hPanx1-injected *Xenopus* oocytes despite the latter displaying significantly increased membrane current (40). However, they used 10 times higher Etd+ concentration, which could explain a large part of these differences. Furthermore, it is possible that the presence of amino acids 371 to 378 partly explains these differences in permeability. Chekeni and colleagues suggested that the uptake of dyes commonly associated with cell death, such as PI or TO-PRO3, is reliant on Panx1 activity (33). Although this hypothesis cannot be excluded, in our acute experiments this dye did not pass through truncated Panx1 HCs even after activating them with pH 8.5.

Under pathological conditions that activate Casp3/7, hPanx1 may undergo cleavage, thereby enhancing hemichannel activity. Here, this enhancement was observed in DAPI uptake assays after exposure to alkaline pH. This greater DAPI permeability concurs with previous reports indicating that irreversible cleavage of hPanx1 generates a constitutively active hemichannel (34). However, a notable difference was the possibility of permeating Ca^{2+}, which does not occur in fl-hPanx1. Furthermore, our results showed that hPanx1 cleavage does not by itself result in greater Ca^{2+} influx before the hemichannel stimulation with alkaline pH (Figs. 3 *B* and *D* and 4*E*). This is closely related to the fact that, according to our molecular simulations and potential of mean force calculations, although the energetic barrier to take up Ca^{2+} through Δ371hPanx1 was much closer to spontaneity compared to fl-hPanx1, it was not null, a stimulus being necessary. Nevertheless, our estimation of Ca^{2+} permeation events and the calculation of the ion density in the pore channel support the fact that caspase-cleaved hPanx1 favors this process.

Mechanistically, we and others have reported that an increase in intracellular free Ca^{2+} concentration enhances hPanx1 HC activity (48–50). However, we did not detect an increase in Ca^{2+} signal after exposing HeLa-hPanx1 cells to pH 8.5, suggesting that extracellular alkaline pH increases the activity of these HCs through a mechanism not related to the activation of a Ca^{2+} permeable channel or Ca^{2+} release from intracellular stores. This was confirmed by determining changes in cytoplasmic Ca^{2+} in the absence of divalent cations and inhibiting IP$_3$R. Interestingly, a massive influx of Ca^{2+} induced by A23187 was sufficient to increase the activity of hemichannels and enhance hPanx1 cleavage, which could favor an even greater entry of this ion. Although it is most likely that Ca^{2+}-induced hPanx1 cleavage depends on caspase activity, it is interesting to note that incubation with Krebs pH 8.5 induced a slight Casp3 activation without affecting Panx1 cleavage.

It has been suggested that hemichannels could favor the inflow of Ca^{2+} that activates proteolytic pathways under different pathological conditions. In turn, intracellular Ca^{2+} overload is a common change in cells undergoing a pathological condition and is known to activate numerous metabolic pathways that lead to ROS generation. For example, Ca^{2+}-dependent lipases generate arachidonic acid, which is then metabolized by lipoxygenases and cyclooxygenases (51) and activates NADPH diaphorase (52), generating superoxide anions. The Ca^{2+} overload also promotes the mitochondrial transition pore formation, leading to a collapse of the electrochemical potential that drastically reduces ATP generation and intensifies the generation of ROS (52).

Despite all this evidence and the fact that the relationship between Ca^{2+} and reactive oxygen/nitrogen species (ROS/RNS) is well established, we did not find that the onset of cell death following Δ371hPanx1 HC opening largely depends on oxidative stress. However, a slight increase in ROS production was detected in Δ371hPanx1 cells exposed to pH 8.5, but only for longer periods. This suggests that although the generation of ROS does not appear to be a cause of this type of cell death, it is a consequence. Moreover, in Δ371hPanx1 cells without extracellular Ca^{2+}, we did not detect a variation in ROS production and cell death upon exposure to pH 8.5, supporting that Ca^{2+} influx was necessary for these effects.

It cannot be underestimated that an increase in Ca^{2+} has also been related to positive cellular mechanisms, such as membrane repair in some types of cell death (24). Furthermore, in a cellular context, Panx1 is usually coexpressed with one or several other Cx HCs also permeable to Ca^{2+}, where the extracellular Ca^{2+} reduces the open probability of Cx HCs. For instance, Cx43 HCs have a pore diameter of ~1.8 nm, aligning with the closed channel conformation. Conversely, reducing extracellular Ca^{2+} to 0 mM increases the pore diameter to ~2.5 nm, indicative of an opened state (53).

In summary, our results suggest that Panx1 HC truncation is a key event in pathological processes involving cell death, which changes channel permeability to small molecules and enhances Ca^{2+} influx to compromised cells. Future studies will clarify whether physiologically relevant molecules or ions other than Ca^{2+} can permeate Panx1 HCs after cleavage of its C-terminal tail. Nielsen et al. proposed that HCs formed by hPanx1 cleaved at residue 378 allow an influx of lactate and glutamate but not glucose, contrasting with HCs formed by the fl-Panx1. This suggests a prevalence of permeation by anionic molecules (40). However, here we demonstrated that Ca^{2+} influx through Δ371hPanx1 HCs favors caspase-dependent cell death. Thus, we propose that the opening of hemichannels formed by Δ371hPanx1 HCs leads to Ca^{2+} influx, which activates proteases (i.e., Casp3) and enhances the C-terminal cleavage of fl-hPanx1. The enrichment of truncated hemichannels with a bigger pore and enhanced hemichannel activity results in intracellular Ca^{2+} overload and subsequent cell death (Fig. 5). These results highlight the role of these hemichannels as a therapeutic target to modulate cell survival.
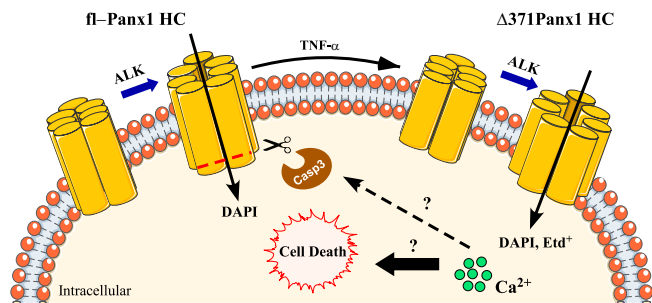
Fig. 5. C-terminal cleaved hPanx1 HCs allow Ca^{2+} influx, which favors cell death. Under exposure to alkaline pH (ALK), fl-hPanx1 HCs increase their activity allowing the influx of small molecules and dyes such as DAPI. Under apoptotic circumstances, the C-terminal tail of Panx1 is proteolyzed by caspase-3 (Casp3), increasing the radius of the pore of the hemichannel, allowing the influx of Ca^{2+} and larger dyes (DAPI and Etd$^+$). Through still unexplored mechanisms, the increase in intracellular Ca^{2+} in turn favors greater cleavage of hPanx1, intracellular Ca^{2+} overload, and ultimately cell death by apoptosis.

Materials and Methods

Plasmid Vectors. PANX1 CRISPR gRNA 1_pSpCas9 BB-2A-Puro (PX459) v2.0 vector was purchased from Genescript, carrying on a gRNA (GCT GCG AAA CGC CAG AAC AG) targeting exon 2 of hPanx1 (on target score of 67, off target 0). pIRES2GFP-hPanx1 was kindly provided by Felix Bukauskas (Department of Neuroscience, Albert Einstein College of Medicine, NY). pIRES2GFP-Δ371hPanx1 vector was prepared through PCR and subcloning product between NheI and EcoRI restriction sites of pIRES2GFP vector, using specific primers as follows: Fw: 5′-GCT AGC ATG GCC ATC GCT CAA CTG -3′; Rev: 5′-GAA TTC TCA GCC AAG GTT TGT CAG GAG T -3′. Reverse primer incorporates a codon stop immediately after Gly371 of hPanx1, before ^{376}DVVD^{379} cleavage motif. hPanx1-mcherry vector was a gift from Agustin Martínez (Instituto de Neurociencias, Universidad de Valparaíso, Valparaíso, Chile).

Cell Cultures. HeLa-parental cells, Panx1$^{-/-}$ HeLa cells, and HeLa cells transiently transfected with fl-hPanx1 or Δ371hPanx1 were used. HeLa-parental cells were obtained from ATCC (Manassas, VA). Panx1$^{-/-}$ HeLa cells were prepared by CRISPR/Cas9 approach, through transfection with an all-in-one vector targeting hPanx1 exon 2 (Genescript) and clone selection with 5 µg/mL puromycin. Complete hPanx1-KO in HeLa cells was demonstrated by western blot analysis. All cells were cultured in plastic tissue culture dishes (Nunc, NY, 14625 USA) in DMEM (Gibco, DK-4000 Roskilde, Denmark), supplemented with 10% fetal bovine serum (Gibco), and kept in incubators at 37 °C with 5% CO_2 and 95% relative humidity. Subconfluent cultures (~70%) were used in all experiments.

Extracellular Alkaline Solution. Cells were bathed with saline Krebs-Ringer solution containing (in mM): 145 NaCl, 5 KCl, 3 $CaCl_2$, 1 $MgCl_2$, 10 glucose, and 10 HEPES, pH 7.4 or pH 8.5. In some experiments, the same combination was used but in the absence of Ca^{2+}. The final pH of each solution was adjusted to the desired final value using TRIS-base.

Dye Uptake Assay. To assay HC permeability changes, we performed dye uptake experiment as previously described (47). In brief, cells were transfected using Turbofect^{TM} transfection reagent and after 24 h they were used in time-lapse dye uptake experiments. HeLa transfectant cells were bathed with Krebs-Ringer solution (pH 7.4 or pH 8.5) containing 5 µM DAPI, 5 µM ethidium (Etd$^+$) bromide, 5 µM PI or 100 nM Sytox. In some experiments, the Panx1 HC activity was evaluated by blocking them with 10 µM CBX or 200 µM ^{10}Panx1 (4). The fluorescence intensity was recorded in the nuclei of at least 20 cells and images were captured every 15 s using the corresponding filter array. To induce mechanical stretch, 6 mL of buffer was dropped onto the cells in drip mode from 10 cm high, as previously reported (54).

Intracellular Ca^{2+} Signal. Cells cultured under the same conditions described above were loaded for 30 min at 37 °C with FURA-2 AM (5 µM). After 10 additional minutes at room temperature (de-esterification period), the intracellular Ca^{2+} signal was evaluated as described previously (55). The protocol for Ca^{2+} imaging involved data collection every 3 s (emission at 510 nm) at 340 and 380 nm

excitation wavelengths using a conventional Nikon Eclipse Ti fluorescent microscope (Nikon, Tokyo, Japan). The Ca^{2+} signal was established as the 340/380 ratio. The area under the curve (AUC) for different segments was calculated in GraphPad Prism. In addition, submembranous Ca^{2+} influx was evaluated in cells cotransfected with genetically engineered Ca^{2+} sensor Lck-GcampP3 (Addgene), which allowed time-lapse recording of Ca^{2+} uptake (ex/em of 480/510 nm). The data collection was taken every 3 s in an inverted fluorescence microscope and the values were plotted as $\Delta F/F_o$ over time.

Western Blot. For protein analysis, cells were homogenized in a M-PER mammalian protein extraction buffer supplemented with a complete protease and phosphatase inhibitor cocktail (ThermoFisher Scientific) and then sonicated three times on ice at 300 W (Sonics & Material INC, VCF1, Connecticut, USA) for 10 s. After centrifugation at 8,000 × g for 10 min, the suspended proteins were quantified and resolved by SDS-PAGE (50 µg/lane) in a 10% (w/v) polyacrylamide gel, transferred to nitrocellulose membranes and probed with a rabbit anti-Panx1 (1:2,000, Abcam), a rabbit anti-active Casp3 (1:1,000, Abcam), or mouse anti-α tubulin (1:5,000, Santa Cruz Biotechnology) antibodies. After extensive washes, the membranes were incubated for 2 h at 4 °C with peroxidase-labeled anti-rabbit or anti-mouse IgG (1:5,000; Jackson ImmunoResearch). The reaction was developed using an enhanced chemiluminescence (ECL) western blot analysis system (Amersham Biosciences). Negative controls consisted of incubating the membrane in the absence of primary antibodies. Anti-Panx1 antibody specificity was demonstrated in protein extracts from Panx1KO HeLa cells.

Quantification of Cell Death. Dead cells were recognized by their staining with PI (5 µM) or Sytox green (30 nM), two molecules that do not significantly permeate Cx HCs or Panx1 HCs [(37); Fig. 1F]. To do this, HeLa cells were seeded in 96-well dishes, 24 h-transfected with each vector, and then exposed for 4 h to either Krebs-Ringer solution at pH 7.4 or 8.5, with or without Ca^{2+} at 37 °C, either in the presence of Sytox green (fl-hPanx1) or PI (Δ371hPanx1). When cell death inhibitors were assayed, they were applied 1 h before stimulations. Immediately after, the plates were placed in the IncuCyte S3 real-time monitoring system (Sartorius AG, Göttingen, Germany) and configured to acquire 4 images per well with the 10× objective, in phase contrast, FITC and Texas Red channels every 1 h for 4 h. Kinetic death analyses were performed automatically with the "cell by cell" processing and segmentation module (Sartorius # 9600-0031), where the number of dead cells (Sytox$^+$/PI$^+$) was constantly divided by the total number of cells in each image.

Quantification of Cellular ROS. The generation of cellular ROS was done in the IncuCyte S3 real-time monitoring system. Cells (2 × 10^5/well) were seeded in a 96-well plate and transfected with Δ371hPanx1 bicistronic vector for 24 h. Nontransfected HeLa-Panx1$^{-/-}$ cells were used as control. Then, cells were exposed to either Krebs-Ringer solution at pH 7.4 or 8.5, with or without Ca^2, in the presence of 1 µM Cellrox deepRed. Immediately after, the plates were placed in the IncuCyte S3 system and configured to acquire 4 images per well with the 10× objective, in phase contrast and Texas Red channels every 1 h for 4 h.

Molecular Dynamics and Potential of Mean Force Calculations. The full-length hPanx1 HC released was considered for this study (PDB ID: 7DWB)(56) as we previously described (47). A C-terminal region, starting from the 371 residue was removed in the truncated protein Δ371hPanx1. Both structures hPanx1 and Δ371hPanx1 were placed in a patch of 1-palmitoyl-2-oleoyl-sn-glycero-3-phosphocholine (POPC). Water molecules were added and neutralized with a concentration of 0.15 mol/L KCl. Dimensions of the final system were 197 x 200 x 292 Å^3 and a total of 890,063 atoms. Amber19sb force field was used to model both proteins (57), the LIPID 17 force field for POPC molecules (58), the TIP3P model for water (59), and ion parameters reported by Joung and Cheatham (60). Visual Molecular Dynamics (VMD) software was used to establish the systems and run analysis (61). AMBER 22 software (62) was used to perform an energy minimization and subsequent equilibration protocol by 50 ns under NPT ensemble at 310 K. Van der Waals interactions were cut off at 10 Å, taking into consideration the dispersion correction for energy and pressure. Electrostatic interactions were computed using particle mesh Ewald under periodic boundary conditions (63), with a cutoff of 10 Å. To keep a constant temperature at 310 K, the velocity rescale (v-rescale) thermostat (64) was employed. To maintain the pressure at 1 bar, the semi-isotropic Berendsen barostat (65) was used.

To evaluate the ability of Ca^{2+} ions to translocate hPanx1 and Δ371hPanx1, the free energy profile or potential of mean force was estimated employing

the umbrella sampling method (66). Two systems were considered using either hPanx1 or Δ371hPanx1 HCs. A Ca^{2+} ion was placed in the extracellular side of the system and restrained using a harmonic restrain of 10 kcal/mol*Å² during a 100 ns equilibration stage. Subsequently, to simulate the translocation of the cation across the protein, the reaction coordinate ξ for the umbrella sampling method was defined as the distance between the center of mass of the cation and the center of mass of seven alpha carbons of residues located in the intracellular section of the protein (sequence PPGVTENVGQS), projected in the Z axis. The reaction coordinate was divided into 35 windows of 1 Å. The force constant of the harmonic spring was 10 kcal/mol*Å² for all windows. At least 30 ns were run for each window, resulting in about 1,050 ns of simulation for each system. The PMF profiles were calculated using the weighted histogram analysis method (WHAM) (67). All simulations were run using the AMBER package. Electrostatics maps were obtained in Maestro software (Schrödinger, Maestro, Schrödinger, LLC, New York, NY, 2021) for visualization and APBS software for calculation (68).

Permeation Events and Density Analysis. To perform Ca^{2+} permeation events analysis and Ca^{2+} density analysis, full-length Panx1 and a truncated Δ371hPanx1, both obtained from PDB ID: 7DWB, were assessed in a 1,000 ns simulation with HMR (69). Both simulations were performed with NAMD (70) and the CHARMM (71) force field. The ion-in-water system built was 2 mol/L $CaCl_2$ in a $120 \times 120 \times 150$ Å³ box with a POPC membrane. The TIPS3P water model was generated according to the CHARMM force field. NPT ensembles were established by integrating the Langevin dynamics with a time-step of 4 fs. The temperature was maintained at 310 K and the electrostatic interactions were recorded using particle mesh Ewald under periodic boundary conditions, with a cutoff of 12 Å. For the imposition of a −135 mV electric field in the Z axis, an electric field of −0.0235 kcal/mol/Å/e was applied. A constant pressure control was applied.

To count the Ca^{2+} permeation events, we split the simulation into four intervals of 250 ns to fill the pore and to calculate the total sum of permeation events in both channels with 70 Å to −70 Å boundaries using the script provided by Cohen et al. (72). To analyze the 3D probability density, VMD's Volmap plugin (73) was used to calculate the average density in all the combined frames. An isovalue of 0.00001 was set to visualize the map.

Image Analysis and Statistical Analysis. Image analysis was mainly done automatically by Incucyte 2019B software. For other analyses, we used the ImageJ 1.64r software (Bethesda, MD, EE.UU.). Graphs and statistical analyses were done with GraphPad Prism 8 software (San Diego, California, EE.UU.). Significance was determined using a one-way ANOVA followed by Kruskal–Wallis or Mann–Whitney post hoc tests, as indicated in the corresponding figure legends. When comparisons were done between two groups, a standard Student's t test was used. In all cases, normal distributions were assumed, and $P \leq 0.05$ was considered statistically significant.

Data, Materials, and Software Availability. The dataset for molecular systems, which includes structure and topology files for AMBER software, configuration files to run the Umbrella Sampling method, and the calculation of the potential of mean force (PMF) for Ca^{2+} translocation through hemichannels, has been deposited in Zenodo (https://zenodo.org/records/11372364 and https://zenodo.org/records/11388204) (74, 75). All other data are included in the article and/or *SI Appendix*.

1. P. Phelan *et al.*, Innexins: A family of invertebrate gap-junction proteins. *Trends Genet.* **14**, 348–349 (1998).
2. S. Penuela, R. Gehi, D. W. Laird, The biochemistry and function of pannexin channels. *Biochim. Biophys. Acta* **1828**, 15–22 (2013).
3. E. C. Beyer, V. M. Berthoud, Gap junction gene and protein families: Connexins, innexins, and pannexins. *Biochim. Biophys. Acta Biomembr.* **1860**, 5–8 (2018).
4. R. Bruzzone, S. G. Hormuzdi, M. T. Barbe, A. Herb, H. Monyer, Pannexins, a family of gap junction proteins expressed in brain. *Proc. Natl. Acad. Sci. U.S.A.* **100**, 13644–13649 (2003).
5. K. Michalski *et al.*, The Cryo-EM structure of pannexin 1 reveals unique motifs for ion selection and inhibition. *Elife* **9**, e54670 (2020).
6. S. Bruzzone, L. Guida, E. Zocchi, L. Franco, A. De Flora, Connexin 43 hemi channels mediate Ca^{2+}-regulated transmembrane NAD+ fluxes in intact cells. *FASEB J.* **15**, 10–12 (2001).
7. S. Rana, R. Dringen, Gap junction hemichannel-mediated release of glutathione from cultured rat astrocytes. *Neurosci. Lett.* **415**, 45–48 (2007).
8. M. A. Riquelme *et al.*, The ATP required for potentiation of skeletal muscle contraction is released via pannexin hemichannels. *Neuropharmacology* **75**, 594–603 (2013).
9. Z. C. Ye, M. S. Wyeth, S. Baltan-Tekkok, B. R. Ransom, Functional hemichannels in astrocytes: A novel mechanism of glutamate release. *J. Neurosci.* **23**, 3588–3596 (2003).
10. D. Lu, S. Soleymani, R. Madakshire, P.A. Insel, ATP released from cardiac fibroblasts via connexin hemichannels activates profibrotic P2Y2 receptors. *FASEB J.* **26**, 2580–2591 (2012).
11. J. A. Orellana *et al.*, Glucose increases intracellular free Ca^{2+} in tanycytes via ATP released through connexin 43 hemichannels. *Glia* **60**, 53–68 (2012).
12. J. Chi *et al.*, Pathogenic connexin-31 forms constitutively active hemichannels to promote necrotic cell death. *PLoS One* **7**, e32531 (2012).
13. J. E. Contreras *et al.*, Metabolic inhibition induces opening of unapposed connexin 43 gap junction hemichannels and reduces gap junctional communication in cortical astrocytes in culture. *Proc. Natl. Acad. Sci. U.S.A.* **99**, 495–500 (2002).
14. J. A. Orellana *et al.*, Hypoxia in high glucose followed by reoxygenation in normal glucose reduces the viability of cortical astrocytes through increased permeability of connexin 43 hemichannels. *Glia* **58**, 329–343 (2010).
15. Q. Ren *et al.*, Cataract-causing mutation of human connexin 46 impairs gap junction, but increases hemichannel function and cell death. *PLoS One* **8**, e74732 (2013).
16. X. Yin *et al.*, Roles of astrocytic connexin-43, hemichannels, and gap junctions in oxygen-glucose deprivation/reperfusion injury induced neuroinflammation and the possible regulatory mechanisms of salvianolic acid B and carbenoxolone. *J. Neuroinflammation* **15**, 97 (2018).
17. L. Zhang *et al.*, Role for nitric oxide in permeability of hippocampal neuronal hemichannels during oxygen glucose deprivation. *J. Neurosci. Res.* **86**, 2281–2291 (2008).
18. J. A. Orellana *et al.*, ATP and glutamate released via astroglial connexin 43 hemichannels mediate neuronal death through activation of pannexin 1 hemichannels. *J. Neurochem.* **118**, 826–840 (2011).
19. W. Shi, M. A. Riquelme, S. Gu, J. X. Jiang, Connexin hemichannels mediate glutathione transport and protect lens fiber cells from oxidative stress. *J. Cell Sci.* **131**, jcs212506 (2018).
20. D. Bano, P. Nicotera, Ca^{2+} signals and neuronal death in brain ischemia. *Stroke* **38**, 674–676 (2007).
21. A. P. Goncalves *et al.*, Activation of a TRP-like channel and intracellular Ca^{2+} dynamics during phospholipase-C-mediated cell death. *J. Cell Sci.* **127**, 3817–3829 (2014).
22. D. J. McConkey, P. Hartzell, P. Nicotera, S. Orrenius, Calcium-activated DNA fragmentation kills immature thymocytes. *FASEB J.* **3**, 1843–1849 (1989).
23. M. J. Berridge, P. Lipp, M. D. Bootman, The versatility and universality of calcium signalling. *Nat. Rev. Mol. Cell Biol.* **1**, 11–21 (2000).
24. L. Pedrera, U. Ros, A. J. Garcia-Saez, Calcium as a master regulator of ferroptosis and other types of regulated necrosis. *Cell Calcium* **114**, 102778 (2023).
25. B. Zhivotovsky, S. Orrenius, Calcium and cell death mechanisms: A perspective from the cell death community. *Cell Calcium* **50**, 211–221 (2011).
26. Y. N. Gong, C. Guy, J. C. Crawford, D. R. Green, Biological events and molecular signaling following MLKL activation during necroptosis. *Cell Cycle* **16**, 1748–1760 (2017).
27. U. Ros *et al.*, Necroptosis execution is mediated by plasma membrane nanopores independent of calcium. *Cell Rep.* **19**, 175–187 (2017).
28. A. B. Santa Cruz Garcia, K. P. Schnur, A. B. Malik, G. C. H. Mo, Gasdermin D pores are dynamically regulated by local phosphoinositide circuitry. *Nat. Commun.* **13**, 52 (2022).
29. K. A. Schalper *et al.*, Connexin 43 hemichannels mediate the Ca^{2+} influx induced by extracellular alkalinization. *Am. J. Physiol. Cell Physiol.* **299**, C1504–C1515 (2010).
30. M. C. Fiori *et al.*, Permeation of calcium through purified connexin 26 hemichannels. *J. Biol. Chem.* **287**, 40826–40834 (2012).
31. F. Vanden Abeele *et al.*, Functional implications of calcium permeability of the channel formed by pannexin 1. *J. Cell Biol.* **174**, 535–546 (2006).
32. P. A. Harcha *et al.*, Pannexin-1 channels are essential for mast cell degranulation triggered during type i hypersensitivity reactions. *Front. Immunol.* **10**, 2703 (2019).
33. F. B. Chekeni *et al.*, Pannexin 1 channels mediate "find-me" signal release and membrane permeability during apoptosis. *Nature* **467**, 863–867 (2010).
34. J. K. Sandilos *et al.*, Pannexin 1, an ATP release channel, is activated by caspase cleavage of its pore-associated C-terminal autoinhibitory region. *J. Biol. Chem.* **287**, 11303–11311 (2012).
35. D. Yang, Y. He, R. Munoz-Planillo, Q. Liu, G. Nunez, Caspase-11 requires the pannexin-1 channel and the purinergic P2X7 pore to mediate pyroptosis and endotoxic shock. *Immunity* **43**, 923–932 (2015).
36. D. B. Hansen, T. H. Braunstein, M. S. Nielsen, N. MacAulay, Distinct permeation profiles of the connexin 30 and 43 hemichannels. *FEBS Lett.* **588**, 1446–1457 (2014).
37. J. A. Orellana *et al.*, Cation permeation through connexin 43 hemichannels is cooperative, competitive and saturable with parameters depending on the permeant species. *Biochem. Biophys. Res. Commun.* **409**, 603–609 (2011).
38. A. A. Vargas *et al.*, On biophysical properties and sensitivity to gap junction blockers of connexin 39 hemichannels expressed in hela cells. *Front Physiol.* **8**, 38 (2017).
39. Y. Yang *et al.*, Endothelial pannexin 1 channels control inflammation by regulating intracellular calcium. *J. Immunol.* **204**, 2995–3007 (2020).
40. B. S. Nielsen *et al.*, Pannexin 1 activation and inhibition is permeant-selective. *J. Physiol.* **598**, 361–379 (2020).
41. N. Hussain *et al.*, Structural insights into the organization and channel properties of human Pannexin isoforms 1 and 3. bioRxiv [Preprint] (2022). https://doi.org/10.1101/2022.09.09.507385 (Accessed 10 January 2024).
42. E. Shigetomi, S. Kracun, B. S. Khakh, Monitoring astrocyte calcium microdomains with improved membrane targeted GCaMP reporters. *Neuron Glia Biol.* **6**, 183–191 (2010).
43. A. De Luisi, A. M. Hofer, Evidence that Ca^{2+} cycling by the plasma membrane Ca^{2+}-ATPase increases the "excitability" of the extracellular Ca^{2+}-sensing receptor. *J. Cell Sci.* **116**, 1527–1538 (2003).
44. Y. Berda-Haddad *et al.*, Sterile inflammation of endothelial cell-derived apoptotic bodies is mediated by interleukin-1alpha. *Proc. Natl. Acad. Sci. U.S.A.* **108**, 20684–20689 (2011).

45. S. Kurtenbach et al., Pannexin1 channel proteins in the zebrafish retina have shared and unique properties. PLoS One 8, e77722 (2013).

46. G. K. Schwalfenberg, The alkaline diet: Is there evidence that an alkaline pH diet benefits health? J. Environ. Public Health 2012, 727630 (2012).

47. X. López et al., A physiologic rise in cytoplasmic calcium ion signal increases pannexin1 channel activity via a C-terminus phosphorylation by CaMKII. Proc. Natl. Acad. Sci. U.S.A. 118, e2108967118 (2021).

48. S. Locovei, J. Wang, G. Dahl, Activation of pannexin 1 channels by ATP through P2Y receptors and by cytoplasmic calcium. FEBS Lett. 580, 239–244 (2006).

49. J. A. Orellana, T. D. Montero, R. von Bernhardi, Astrocytes inhibit nitric oxide-dependent Ca^{2+} dynamics in activated microglia: Involvement of ATP released via pannexin 1 channels Glia 61, 2023–2037 (2013).

50. N. Prochnow et al., Pannexin1 in the outer retina of the zebrafish, Danio rerio. Neuroscience 162, 1039–1054 (2009).

51. J. C. Sáez, J. A. Kessler, M. V. Bennett, D. C. Spray, Superoxide dismutase protects cultured neurons against death by starvation. Proc. Natl. Acad. Sci. U.S.A. 84, 3056–3059 (1987).

52. S. K. Powers, J. Duarte, A. N. Kavazis, E. E. Talbert, Reactive oxygen species are signalling molecules for skeletal muscle adaptation. Exp. Physiol. 95, 1–9 (2010).

53. J. Thimm, A. Mechler, H. Lin, S. Rhee, R. Lal, Calcium-dependent open/closed conformations and interfacial energy maps of reconstituted hemichannels. J. Biol. Chem. 280, 10646–10654 (2005).

54. X. López et al., Stretch-induced activation of pannexin 1 channels can be prevented by PKA-dependent phosphorylation. Int. J. Mol. Sci. 21, 9180 (2020).

55. L. A. Cea et al., Skeletal muscle atrophy induced by diabetes is mediated by non-selective channels and prevented by boldine. Biomolecules 13, 708 (2023).

56. S. Zhang et al., Structure of the full-length human Pannexin1 channel and insights into its role in pyroptosis. Cell Discov. 7, 30 (2021).

57. C. Tian et al., ff19SB: Amino-acid-specific protein backbone parameters trained against quantum mechanics energy surfaces in solution. J. Chem. Theory Comput. 16, 528–552 (2020).

58. C. J. Dickson et al., Lipid14: The amber lipid force field. J. Chem. Theory Comput. 10, 865–879 (2014).

59. W. L. Jorgensen, J. Chandrasekhar, J. D. Madura, R. W. Impey, M. L. Klein, Comparison of simple potential functions for simulating liquid water. J. Chem. Phys. 79, 926–935 (1983).

60. I. S. Joung, T. E. Cheatham III, Determination of alkali and halide monovalent ion parameters for use in explicitly solvated biomolecular simulations. J. Phys. Chem. B 112, 9020–9041 (2008).

61. W. Humphrey, A. Dalke, K. Schulten, VMD: Visual molecular dynamics. J. Mol. Graph. 14, 27–38 (1996).

62. D. A. Case et al., The Amber biomolecular simulation programs. J. Comput. Chem. 26, 1668–1688 (2005).

63. T. Darden, D. York, L. Pedersen, Particle mesh Ewald: An N·log(N) method for Ewald sums in large systems. J. Chem. Phys. 98, 10089–10092 (1993).

64. G. Bussi, D. Donadio, M. Parrinello, Canonical sampling through velocity rescaling. J. Chem. Phys. 126, 014101 (2007).

65. H. J. C. Berendsen, J. P. M. Postma, W. F. van Gunsteren, A. DiNola, J. R. Haak, Molecular dynamics with coupling to an external bath. J. Chem. Phys. 81, 3684–3690 (1984).

66. B. Roux, The calculation of the potential of mean force using computer simulations. Comput. Phys. Commun. 91, 275–282 (1995).

67. S. Kumar, J. M. Rosenberg, D. Bouzida, R. H. Swendsen, P. A. Kollman, THE weighted histogram analysis method for free-energy calculations on biomolecules. I. The method. J. Comput. Chem. 13, 1011–1021 (1992).

68. N. A. Baker, D. Sept, S. Joseph, M. J. Holst, J. A. McCammon, Electrostatics of nanosystems: Application to microtubules and the ribosome. Proc. Natl. Acad. Sci. U.S.A. 98, 10037–10041 (2001).

69. C. W. Hopkins, S. Le Grand, R. C. Walker, A. E. Roitberg, Long-time-step molecular dynamics through hydrogen mass repartitioning. J. Chem. Theory Comput. 11, 1864–1874 (2015).

70. J. C. Phillips et al., Scalable molecular dynamics on CPU and GPU architectures with NAMD. J. Chem. Phys. 153, 044130 (2020).

71. J. Lee et al., CHARMM-GUI input generator for NAMD, GROMACS, AMBER, OpenMM, and CHARMM/OpenMM simulations using the CHARMM36 additive force field. J. Chem. Theory Comput. 12, 405–413 (2016).

72. J. Cohen, A. Arkhipov, R. Braun, K. Schulten, Simulation of water permeation through nanotubes (2012), NAMD tutorial available at http://www.ks.uiuc.edu/Training/Tutorials.

73. J. Cohen, F. Zhu, E. Tajkhorshid, Z. Huang, Imaging the migration pathways for O2, CO, NO, and Xe inside myoglobin. Biophys. J. 91, 1844–1857 (2006).

74. M. Salgado et al., Dataset of molecular structures of PNAS article "Ca^{2+} permeation through C-terminal cleaved, but not full-length human Pannexin1 hemichannels, mediates cell death". Zenodo. https://zenodo.org/records/11372364. Deposited 28 May 2024.

75. M. Salgado et al., General dataset of PNAS article "Ca^{2+} permeation through C-terminal cleaved, but not full-length human Pannexin1 hemichannels, mediates cell death". Zenodo. https://zenodo.org/records/11388204. Deposited 29 May 2024.